

1                   **Assessing the Impact of Meteorological History**

2                                   **on Subtropical Cloud Fraction**

3                                   **GUILLAUME S. MAUGER AND JOEL R. NORRIS \***

*Scripps Institution of Oceanography, La Jolla, California*

---

\* *Corresponding author address:* Joel R. Norris, Scripps Institution of Oceanography, 9500 Gilman Dr,  
MC 0224, La Jolla, CA 92093-0224.

E-mail: jnorris@ucsd.edu

4 ABSTRACT

5 This study presents findings from the application of a new Lagrangian method used to eval-  
6 uate the meteorological sensitivities of subtropical clouds in the northeast Atlantic. Parcel  
7 back trajectories are used to account for the influence of previous meteorological condi-  
8 tions on cloud properties, while forward trajectories highlight the continued evolution of  
9 cloud state. Satellite retrievals from MODIS, CERES, QuikScat, and SSM/I provide mea-  
10 surements of cloud properties as well as atmospheric state. These are complemented by  
11 meteorological fields from the ECMWF operational analysis model. Observations are com-  
12 posed by cloud fraction, and mean trajectories are used to evaluate differences between  
13 each composite.

14  
15 Systematic differences in meteorological conditions are found to extend through the full  
16 144-hour trajectories, confirming the need to account for cloud history in assessing impacts on  
17 cloud properties. The findings associate increased lower tropospheric stability (LTS), cooler  
18 SSTs, a more humid free troposphere, stronger cold advection, and a decrease in divergence  
19 with an increase in cloud fraction. Most striking among these is the observation that large,  
20 synoptic-scale variations in divergence appear to exert a dominant influence on cloud cover.  
21 Consistent with prior work, we find that cloud cover variations correlate best with variations  
22 in LTS and SST that are 36 hours upwind. In addition, we find that free tropospheric  
23 humidity, along-trajectory SST gradient, and surface fluxes all correlate best at lags ranging  
24 from 0 to 12 hours. Changes in surface divergence, in contrast, generally lead cloud cover  
25 variations by less than 6 hours. Notably, in the early part of the trajectories several of the  
26 above associations are reversed. In particular, when trajectories computed for small cloud

27 fraction scenes are traced back 72 hours, they are found to originate in conditions of weaker  
28 surface divergence and stronger surface fluxes relative to those computed for large cloud  
29 fraction scenes. Coupled with a drier boundary layer and warmer SSTs, this suggests that a  
30 decoupling of the boundary layer precedes cloud dissipation. We develop an approximation  
31 for the stratification of the boundary layer, and find further evidence that stratification  
32 plays a role in differentiating between developing and dissipating clouds. Overall, cloud  
33 cover appears to be most strongly impacted by variations in surface divergence over short  
34 time-scales (<6 hrs) and by factors influencing boundary-layer stratification over longer  
35 time-scales (12-48 hrs).

## 36 **1. Introduction**

37 It is well established that stratocumulus clouds found over eastern ocean basins exert a  
38 strong cooling effect on the Earth's climate, primarily due to their weak greenhouse effect,  
39 extensive coverage, and high albedo relative to the ocean. As a result, small perturbations  
40 to these clouds have the potential to significantly impact the Earth's energy balance. An  
41 improved understanding of boundary layer cloud sensitivities is necessary to estimate the  
42 magnitude of aerosol-cloud effects, improve current model parameterizations, and properly  
43 assess the consequences of climate change.

44 Prior work indicates that the dynamical forcing of stratocumulus clouds occurs at scales  
45 larger than the mesoscale (Rozendaal and Rossow 2003; Lewis et al. 2004), meaning it is fea-  
46 sible to assess meteorological impacts on cloud properties using large-scale datasets. Norris  
47 and Iacobellis (2005) combined surface observations with meteorological reanalysis data to

48 show that the dominant parameters associated with cloud properties are vertical velocity, ad-  
49 vection, and SST. An earlier study by Klein et al. (1995) combined several decades of surface  
50 observations from the northeast Pacific with radiosonde data and large-scale observations.  
51 They showed that low-cloud amount correlates better with SST and upper air temperature  
52 24 to 30 hours upwind than with the local SST and upper air temperature. These results  
53 imply that stratocumulus clouds have “memory,” or that the history of forcings is an im-  
54 portant determinant of cloud state. This can be interpreted in terms of the time scale for  
55 boundary-layer adjustment, as governed by surface fluxes, entrainment and subsidence rates,  
56 and temperature and humidity profiles of the free troposphere.

57 Accounting for previous meteorological impacts necessitates a Lagrangian perspective on  
58 cloud evolution. In addition to the study by Klein et al. (1995), several other investigations  
59 have evaluated stratocumulus dynamics from a Lagrangian perspective. During the Atlantic  
60 Stratocumulus Transition Experiment (ASTEX) a suite of airborne, ship-based, and balloon  
61 measurements were used to track the Lagrangian evolution of a boundary-layer airmass, with  
62 the goal of investigating the transition from stratocumulus to trade cumulus (Albrecht et al.  
63 1995). Observations made during ASTEX showed that synoptic variability in the northeast  
64 Atlantic cloud field is much greater than that observed off the California coast. Building on  
65 insights gained from ASTEX, Pincus et al. (1997) computed parcel trajectories using 1000  
66 hPa winds to evaluate the downstream evolution of cloud fields in the northeastern Pacific.  
67 Their results were consistent with those of Klein et al. (1995), showing that cloud response  
68 is best correlated with stability at a lag of 16 hours, and suggesting that warming SSTs play  
69 a dual role by thickening clouds over shorter time scales, and accelerating the transition to  
70 trade cumulus over longer time scales.

71 The above studies have provided invaluable information on the meteorological sensitivities  
72 of subtropical clouds. However, all three studies are limited in terms of spatial and temporal  
73 sampling. In the Klein et al. (1995) study, the analysis is centered on a unique ocean  
74 weather station, and therefore cannot be extended to other geographic regions. The in situ  
75 observations of ASTEX and the analysis of Pincus et al. (1997), conversely, cover a fairly  
76 broad geographic region but are severely limited in sample size. A new Lagrangian analysis  
77 method is needed that includes greater flexibility in spatial and temporal sampling, making  
78 it possible to obtain robust statistical estimates of cloud meteorological sensitivities while  
79 allowing greater flexibility to assess different cloud regimes.

80 Mauger and Norris (2007) recently introduced a technique that builds on the above stud-  
81 ies by using global meteorological analyses to compute three-dimensional trajectories. Parcel  
82 back-trajectories are used to identify the previous locations and movement of air within and  
83 above the boundary layer relative to the time of cloud measurements. Satellite observations  
84 and meteorological analysis fields are interpolated onto back trajectory positions, permitting  
85 a Lagrangian perspective on cloud evolution. By focusing uniquely on global datasets, the  
86 new technique allows for broad geographic sampling and a dramatic increase in sample size.

## 87 **2. Methods**

### 88 *a. Study region and dates*

89 The analysis is focused on the subtropical northeast Atlantic. The northeast Atlantic  
90 is chosen because it is a transitional region, and thus exhibits greater variability in cloud

91 fraction. The study region is larger than that of Mauger and Norris (2007), extending from  
92 24N to 40N and 35W to 10W (Figure 1). These bounds are chosen to include all regions  
93 influenced by subtropical clouds while avoiding the heavy dust region west of Africa and the  
94 predominance of extratropical cyclones to the north. The conclusions of this study are not  
95 sensitive to the exact location of the region considered. In order to maximize the statistical  
96 significance of the results, observations are obtained for June through August 2000-2006.

97 *b. Trajectory analysis and data*

98 Here we provide a brief summary of the trajectory technique and the observational data  
99 employed. Parcel back-trajectories are computed from European Centre for Medium range  
100 Weather Forecasting (ECMWF) operational analyses using the Hybrid Single-Particle La-  
101 grangian Integrated Trajectory Model (HYSPLIT). Trajectory calculations are started at  
102 two altitudes, one within and one above the boundary layer (500 and 2000 m), and ex-  
103 tend 72 hours prior to and 72 hours beyond the time of observation. Satellite observations  
104 and meteorological analyses are interpolated onto trajectory positions to obtain estimates of  
105 meteorological conditions.

106 HYSPLIT computes three-dimensional parcel trajectories using a simple advection scheme  
107 and gridded meteorological fields as input. We use ECMWF analysis winds, temperature,  
108 heights and surface pressure as input to HYSPLIT calculations. Stohl and Seibert (1998)  
109 show that trajectory calculations perform well in undisturbed conditions, and that the ma-  
110 jority of error arises in the presence of fronts, where winds and transport are poorly resolved.  
111 Focusing on stratocumulus clouds thus conveniently avoids the dominant sources of error.

112 Although difficult to assess, studies attempting to quantify uncertainty in trajectories gen-  
113 erally center on a position uncertainty of 20% of the distance travelled (Stohl et al. 1998).  
114 The mean displacement for the 72 hour trajectories is 1000 km, which implies a position un-  
115 certainty of approximately 200 km at the trajectory endpoints. In addition to our synoptic  
116 focus, the uncertainty in trajectory position is another reason that low-resolution satellite  
117 fields are chosen for the present analysis. Errors associated with trajectory position are  
118 also unlikely to be systematically biased and will thus be reduced by averaging numerous  
119 trajectories. An important caveat to the use of trajectories is that air parcels do not travel  
120 adiabatically along wind streamlines, but instead mix with their environment. However, the  
121 present analysis is focused on the impact of large-scale meteorological forcings on clouds.  
122 Tests indicate that the length scale of meteorological variations is large enough that mixing  
123 can be neglected.

124 Satellite data are obtained from four different instruments and are used to assess mete-  
125 orological state as well as validate analysis fields. All of the satellite datasets are regridded  
126 from their native resolutions to match the MODIS (Moderate Resolution Imaging Spectro-  
127 radiometer, described below)  $1^\circ \times 1^\circ$  grid. An advantage of the trajectory technique is that  
128 satellite observations need not be coincident in order to provide useful information: ob-  
129 servations are simply interpolated to the times and locations for which data are available.  
130 Overpass times are assigned to the 3-hourly bin that is most representative of overpass times  
131 for the study region and the satellite platform under consideration. Although there will be  
132 small variations in overpass times that are not resolved by the 3-hourly time intervals, these  
133 are not expected to vary systematically with meteorology. A brief overview of each dataset  
134 is provided below – further details regarding data quality, potential sources of bias, and

135 comparisons between independent measurements are discussed at length in Mauger (2008).

136 Cloud microphysical and macrophysical properties are obtained from MODIS as daily  
137 gridded averages (MOD08\_D3, Collection 005) at a resolution of  $1^\circ \times 1^\circ$ . MODIS cloud-top  
138 temperature ( $T_{TOP}$ ) retrievals are made using the  $11 \mu\text{m}$  brightness temperature. Although  
139 MODIS cloud fraction (CF), effective radius ( $R_E$ ), and water path (LWP) retrievals are all  
140 differentiated by cloud phase,  $T_{TOP}$  retrievals are not. In the present study, retrievals of  
141 CF,  $R_E$ , and LWP are only taken for pixels identified as liquid phase clouds. Scenes con-  
142 taining high clouds are not excluded from the present analysis, since doing so could bias the  
143 results (for example, by constraining the upper-level divergence). We use a random overlap  
144 assumption to account for low clouds that are masked by thick high clouds. Tests employing  
145 both minimum and maximum overlap assumptions indicated a negligible sensitivity to the  
146 overlap assumption used. Since high clouds are not common in the present study region,  
147 this does not amount to a large correction.

148 Since MODIS cloud-top temperature retrievals are not differentiated by cloud phase,  
149  $T_{TOP}$  retrievals are biased cold when high clouds are present. Tests, performed by composi-  
150 ting  $T_{TOP}$  against retrievals of high cloud cover, show that high clouds strongly impact the  
151 retrieved cloud top temperature (Mauger 2008, Fig. III.2). As a result,  $T_{TOP}$  observations  
152 are screened for high clouds. High clouds are screened by constraining `Cloud_Fraction_Ice`  
153 to be less than 1% and `Cirrus_Fraction_SWIR` to less than 25% (Platnick et al. 2003), which  
154 together provide a conservative test for high cloud contamination. The high threshold for  
155 `Cirrus_Fraction_SWIR` is chosen because, although useful due to its sensitivity to thin cir-  
156 rus, the authors found evidence that the retrieval is biased high in the presence of bright,  
157 low-level clouds (Mauger 2008).

158 Since the high cloud screening could lead to a sample bias in  $T_{TOP}$ -derived quantities, the  
159 “all-sky” and “no ice” samples were compared for consistency. As expected given a constraint  
160 on high clouds, the “no ice” samples featured a drier free troposphere and stronger surface  
161 divergence. These changes were accompanied by a reduction in latent heat flux, increases in  
162 stability, and a greater distinction in temperature advection between composites. Overall,  
163 however, the relationships present in the “all-sky” cases are all present in those that are  
164 filtered for high clouds. Although not completely interchangeable, our results indicate that  
165 the high cloud filtering does not strongly bias the composites of  $T_{TOP}$ .

166 Several authors have indicated the potential for retrieval biases in pixels that are only  
167 partially covered by cloud (Wielicki and Parker 1992; Matheson et al. 2006). Matheson et al.  
168 (2006) compare threshold cloud retrievals with cloud properties derived from a new method  
169 which accounts for the sub-pixel cloud fraction. Using Advanced Very High Resolution  
170 Radiometer (AVHRR) data at 4-km resolution, their analysis suggests this bias is small  
171 relative to other factors that influence cloud forcing. Tests were performed by compositing  
172  $T_{TOP}$  and  $R_E$  retrievals against low-level cloud fraction (Mauger 2008). These indicate that  
173 partial pixel contamination of  $T_{TOP}$  retrievals is most pronounced for cloud cover less than  
174 about 30%. Variations in effective radius are less straightforward to interpret, though partial  
175 pixel biases appear to only impact retrievals for cloud cover less than 10%.

176 Data from the Clouds and the Earths Radiant Energy System (CERES) instrument, also  
177 aboard Terra, are used to obtain observations of the top-of-atmosphere (TOA) broadband  
178 shortwave flux. This study uses the swath-level Single Scanner Footprint (SSF) product to  
179 obtain observations of scene albedo and top-of-atmosphere radiative flux. Both quantities  
180 are retrieved for all-sky conditions. Only over-ocean observations are included in the present

181 study. Regions of sun-glint and scenes with solar zenith angles greater than  $70^\circ$  are also  
182 excluded from the analysis. Finally, CERES pixels are rejected if the Angular Distribution  
183 Model (ADM), used to convert from directional radiances to hemispheric fluxes, is obtained  
184 from the CERES Artificial Neural Network technique (Loukachine and Loeb 2003) instead  
185 of the standard empirical scene-based ADMs. This is done to maintain consistency between  
186 retrievals.

187 All-sky liquid water path and precipitable water are obtained from the Special Sensor  
188 Microwave Imager (SSM/I) deployed onboard the f15 satellite. The retrieval products are  
189 obtained from Remote Sensing Systems, Inc. using the version 6 (V6) retrieval algorithm.  
190 Mauger (2008) performed a comparison between the SSM/I retrievals of liquid water path  
191 (LWP) and those of MODIS. The agreement was found to be well within the estimated  
192 accuracy of  $25 \text{ g m}^{-2}$  for SSM/I retrievals (Wentz 1997). However, a small systematic bias  
193 was observed, in which SSM/I retrievals of LWP for thin clouds ( $\text{LWP} < 200 \text{ g m}^{-2}$ ) were  
194 systematically larger than those of MODIS. Notably, the disagreement is primarily associated  
195 with the difference in overpass times between the two sensors.

196 Surface divergence is computed from QuikScat 10 m wind retrievals (Level 2B swath).  
197 In this study we use the Level 2B Direction Interval Retrieval with Threshold Nudging  
198 (DIRTH) product from QuikScat. Since the level 2B grid is not orthogonal, we average the  
199 zonal and meridional wind components separately onto a regular grid before computing the  
200 divergence. Rain-flagged retrievals are excluded from the regridding. The analysis of Milliff  
201 et al. (2004) indicates that removal of rain-flagged data does not bias the wind observations  
202 for the region under consideration in this study.

203 Meteorological parameters are obtained from the European Centre for Medium-Range

204 Weather Forecasting (ECMWF) operational analyses. The data is obtained from the Na-  
205 tional Center for Atmospheric Research (NCAR), regrided from T106 spectral resolution  
206 with 21 vertical levels (NCAR 1990). ECMWF is chosen to provide meteorological fields  
207 based on its superior performance in simulating boundary layer development and evolution  
208 (Stevens et al. 2007). In contrast with the reanalysis, the ECMWF operational analysis  
209 includes the most recent model improvements and newly available observations.

210 QuikScat surface winds are assimilated into ECMWF. Recent studies indicate that the  
211 quality of the assimilation is high for divergence (McNoldy et al. 2004; Stevens et al. 2007).  
212 However, given the potential for model influence on ageostrophic motions and near-surface  
213 winds, QuikScat is included in the present study for comparison with ECMWF surface  
214 divergence.

215 *c. Sample selection, composite averages, and confidence intervals*

216 Low-level cloud fraction is chosen as the dependent variable in this study. Cloud fraction  
217 has the advantage of being more straightforward to define observationally relative to other  
218 cloud properties such as water path and cloud albedo. Cloud cover is also commonly used  
219 in sensitivity studies, and exerts the greatest influence on shortwave cloud forcing.

220 Samples are selected randomly from the upper, middle, and lower terciles of cloud frac-  
221 tion. Terciles are chosen for simplicity, though tests indicate that subdividing the data  
222 differently, such as into quartiles or into clear and overcast scenes, does not alter the conclu-  
223 sions of the present study. Sample biases associated with geographic and seasonal variations  
224 in cloudiness could artificially bias the results. In order to eliminate this possibility, the

225 study region is split into 19 grid boxes, each one  $4^\circ$  latitude by  $5^\circ$  longitude (see Figure 1).  
226 These dimensions are consistent with our estimate of the autocorrelation scale, discussed  
227 below. The data are then sampled uniformly from each grid box for each month in order to  
228 maintain even sampling throughout the domain.

229 Composite differences between terciles are used to assess sensitivities. Confidence inter-  
230 vals (95%) in all composites are estimated using a bootstrap method. The bootstrap method  
231 works by sampling with replacement from the pool of trajectories in a particular composite.  
232 A mean is computed from the randomly selected sample and the iteration is repeated 1000  
233 times. This permits an estimation of the probability distribution of outcomes, from which  
234 we obtain our 95% confidence limits.

235 We obtain the autocorrelation scale by estimating the e-folding scale for lagged autocorre-  
236 lations, and find time and length scales of approximately 12 hours and 250 km, respectively.  
237 The decorrelation length is estimated at twice the autocorrelation scale. Using these decor-  
238 relation scales, a second bootstrap method is used to estimate the degrees of freedom in a  
239 sample. We find a consistent sample reduction of a factor of 5. This estimate of the sam-  
240 ple degrees of freedom is implemented in the bootstrap error calculation described above  
241 by reducing the number of points included in each randomly selected composite. With re-  
242 gard to the present analysis, it is important to note the distinction between the Eulerian  
243 autocorrelation described above and the autocorrelation along a Lagrangian trajectory. As  
244 expected, the analysis presented below indicates that the latter time-scale is much longer  
245 than 12 hours.

### 246 3. Results

247 Trajectories are computed for all selected cloud observations, and satellite and analysis  
248 data are interpolated onto trajectory positions. Composites are computed from the roughly  
249 10,000 trajectories that fall into each tercile. Adjusting for autocorrelation between observa-  
250 tions, this represents an effective sample size of 2,000. Confidence limits are estimated using  
251 the bootstrap method described above. Since cloud sensitivities may not vary linearly or even  
252 monotonically with cloud fraction, the middle tercile is included for comparison. Following  
253 the sample selection, the composite trajectories are hereafter referred to as LC (“Large low-  
254 level Cloud fraction”), MC (“Medium low-level Cloud fraction”), and SC (“Small low-level  
255 Cloud fraction”).

#### 256 *a. Cloud Properties*

257 Figure 2 shows a histogram of cloud fraction including data from all three terciles. As  
258 discussed above, low-level cloud fraction is defined using the MODIS retrieval of liquid water  
259 cloud fraction and correcting the retrieval for overlap by high cloud. Clear-sky (CF=0) scenes  
260 are included in the histogram as well as throughout the present study, since they represent  
261 a relevant part of the continuum in cloud cover. As expected for a cloud field with a spatial  
262 autocorrelation-scale greater than the scale at which it is gridded, the distribution is U-  
263 shaped. A more interesting detail is the skewness of the distribution, which shows 2-3 times  
264 as many clear-sky as overcast days. This is consistent with observations made during the  
265 ASTEX campaign, which took place in the same region (Bretherton et al. 1995). The dashed  
266 lines show the average delineation between the 3 terciles. As a result of the skewness, over

267 30% of the SC observations are clear-sky cases. However, as discussed below, the mean of  
268 these small cloud fraction observations represents the endpoint of a continuous decline in  
269 cloud fraction over the course of a 72 hour back trajectory.

270 Figure 3 shows the mean position along each composite trajectory. An indication of the  
271 speed along each trajectory is given by the position of the error bars, which are displayed at  
272 3 hourly intervals. For clarity, only the 500m trajectories are shown. Vertical shear is present  
273 in the trajectories: the 2000m trajectories generally circulate along tighter anticyclonic paths  
274 than those at 500m, showing warmer SSTs and weaker divergence at  $t=-72$  hours and cooler  
275 SSTs and stronger divergence at  $t=+72$  hours relative to those initiated at 500m. However,  
276 the cloud and meteorological differences between composites are qualitatively similar for the  
277 500m and 2000m trajectories, such that focusing uniquely on those at 500m does not impact  
278 the conclusions of this study.

279 All composite trajectories are seen to follow anti-cyclonic paths defined by the climato-  
280 logical high pressure region found over the eastern north Atlantic. There is no significant  
281 distinction between the forward trajectories, where winds are subject to significantly less  
282 synoptic and regional variability. In contrast, the SC back trajectories originate farther  
283 south and west than those for the LC cases. This difference in the trajectories is associated  
284 with a southwest shift in the Azores high for the SC composite.

285 Composite trajectories of low-level cloud fraction and CERES all-sky top-of-atmosphere  
286 net shortwave flux are shown in Figure 4. The differences in low-level cloud fraction are  
287 greatest in the 48 hours surrounding the time of observation ( $t=-24$  to  $t=+24$ ). Notably,  
288 the differences remain significant from the beginning of the trajectory, extending to 48 hours  
289 beyond the time of observation, consistently showing greater cloud cover for the LC compos-

290 ite and less for the SC composite. Cloud cover is also seen to vary non-linearly between the  
291 SC, MC, and LC composites, with the LC case showing a substantial jump in cloud fraction  
292 relative to the MC case. Associated with the changes in low-level cloud fraction, Figure 4  
293 shows the composite trajectories for all-sky, top-of-atmosphere (TOA) net shortwave flux  
294 from CERES ( $F_{SW}$ ). The flux values retrieved from CERES are representative of Terra  
295 overpass times, which occur shortly after noon local time and are thus much larger than the  
296 diurnally averaged fluxes. As expected, shortwave fluxes retrieved from CERES reflect the  
297 strong cooling effect of low-level clouds.

298 Since the interpretation of all-sky liquid water path (LWP) can be somewhat ambiguous,  
299 Figure 5 shows trajectories of MODIS in-cloud and all-sky LWP alongside all-sky LWP from  
300 SSM/I. As discussed above, SSM/I retrievals are consistently larger than those of MODIS  
301 for the range of water paths considered. The scale of this discrepancy increases as cloud  
302 cover decreases, suggesting that a partial pixel bias in the MODIS retrievals is responsible  
303 for the difference. Overall, the retrievals presented in Figure 5 are consistent in associating  
304 increasing water paths with growing cloud decks and the converse for dissipating clouds.

### 305 *b. Thermodynamic conditions*

306 The Lagrangian analysis developed herein is motivated by the observation that cloud  
307 cover correlates best with upwind variations in the stability of the lower atmosphere (*e.g.*,  
308 Klein et al. 1995; Mauger and Norris 2007). Lower tropospheric stability is defined here  
309 as the difference in potential temperature between 700 hPa and the surface ( $\theta_{700} - \theta_{SFC}$ ).  
310 Figure 6 shows that the above observation is confirmed by the present study: the differences

311 in LTS in the earlier parts of the trajectory are greater than at  $t=0$ . Large cloud fraction  
312 cases are associated with a significantly more stable atmosphere, a condition that persists  
313 throughout the course of the 72 hours prior to the time of observation. The greater stability,  
314 due both to a warmer free troposphere and cooler sea surface temperatures (SST), is also  
315 accompanied by an increase in moisture above the boundary layer, as seen in the trajectories  
316 of specific humidity at 700 hPa ( $q_{700}$ ).

317 Figure 7 shows the composite trajectories for the rate of sea surface temperature change  
318 ( $\Delta\text{SST}$ ), 10 m surface wind speed ( $W_{10m}$ ), and sensible ( $F_{SH}$ ) and latent ( $F_{LH}$ ) heat fluxes,  
319 all obtained from ECMWF analyses. The Lagrangian analog of SST advection is simply the  
320 along-trajectory rate of sea surface temperature change. This is equivalent to the conven-  
321 tional definition of temperature advection ( $-v \cdot \nabla T$ ) applied to the trajectory path, and is  
322 therefore hereafter referred to as SST advection. The plots in Figure 7 are displayed in order  
323 of increasing model influence: Surface winds and temperatures are directly observed and  
324 are likely less influenced by the model than surface fluxes. Consequently, more confidence  
325 should be placed in the composite differences in SST advection and surface wind speed.

326 As with LTS, the results are consistent with prior work associating negative temperature  
327 advection with increased incidence of low-level clouds (*e.g.*, Klein et al. 1995). The differences  
328 in  $\Delta\text{SST}$  are greatest between  $t=-24$  and  $t=0$ , however trajectory separation is apparent up  
329 to 48 hours back. Surface winds are also stronger for the LC cases. Increased cold advection  
330 and stronger surface winds will both promote increased surface fluxes, and the SC cases  
331 show significantly weaker surface sensible and latent heat fluxes when compared to the other  
332 two cases. The significant distinction between the SC and MC surface fluxes is contrasted  
333 by the weak distinction between the MC and LC cases. This is partially reflected in the

334  $\Delta$ SST trajectories, and is an indication that cloud sensitivities do not vary linearly with  
335 cloud fraction. Finally, the above relationships are of opposite sign early in the trajectory.  
336 Specifically, in the earliest 24 hours of the trajectories the LC cases are associated with  
337 *decreased* surface fluxes and *weaker* cold advection.

### 338 *c. Large-scale Dynamics*

339 Figure 8 displays the large-scale dynamic influences on cloud fraction. Both QuikScat  
340 retrievals and ECMWF surface divergence are shown to be inversely associated with cloud  
341 fraction. This is an interesting observation, since stratiform clouds are known to exist in  
342 regions that are climatologically defined by strong subsidence. The present results suggest  
343 that these clouds actually exist in a delicate balance between excessively divergent and  
344 insufficiently divergent regimes. Pressure vertical velocity at 700 hPa ( $\omega_{700}$ , from ECMWF) is  
345 consistent with this result, showing a divergent regime overall, but a decrease in cloud fraction  
346 with increasing divergence. Notably, these fields too show a reversal in the relationship with  
347 cloud cover in the early part of the trajectory, showing that prior to  $t=-48$  the LC cases  
348 are subject to greater divergence. An important question is whether the above quantities  
349 constitute a valid proxy for the subsidence rate at cloud top. Estimates of the cloud-top  
350 subsidence rate, using both retrieved cloud-top height and a fixed inversion height, are  
351 consistent with the observed changes in surface divergence, showing weaker subsidence for  
352 the LC case at  $t=0$  but stronger subsidence at  $t=-72$ .

353 *d. Boundary layer properties*

354 A common challenge in remote sensing studies of boundary layer clouds is the estimation  
355 of quantities intrinsic to the boundary layer. These include the inversion height, boundary-  
356 layer stability, and the strength of the inversion. By assuming a particular boundary layer  
357 lapse rate, MODIS retrievals of cloud top temperature can be combined with retrievals of  
358 SST to obtain estimates of boundary layer height ( $Z_{TOP}$ ). Conversely, by specifying an  
359 assumed inversion height, the same information can be used to estimate the boundary layer  
360 lapse rate ( $\Gamma_{BL}$ ). Inspection of the results, shown in Figure 9, provides a means of contrasting  
361 the potential veracity of the constant lapse rate assumption ( $Z_{TOP}$ ) against the assumption  
362 of a constant boundary layer height ( $\Gamma_{BL}$ ).

363 Before proceeding, it should be noted that although all variables derived from MODIS  
364 cloud-top temperature estimates are screened for high clouds, there is no straightforward  
365 correction for partial pixel error. It is thus likely that at least a part of the observed relation-  
366 ship results from the misattribution of partially-filled MODIS pixels as cloudy. Calculations  
367 indicate that correcting for this bias results in a significantly reduced difference between  
368 composites, but does not alter the sign of the association with cloud cover. Nevertheless, it  
369 is likely that some bias exists, and that this bias impacts the observed relationship between  
370 estimates of cloud top temperature and the composites of low-level cloud cover.

371 The trajectory of  $Z_{TOP}$  indicates that the LC case has a shallower inversion early in  
372 the trajectory, which then becomes significantly deeper at the time of observation, and  
373 remains larger than the MC and SC cases through  $t=72$  hours. The changes in  $Z_{TOP}$  are  
374 consistent with the prediction that marine clouds maintain fairly constant entrainment rates

375 [*e.g.*, Schubert et al. 1979], showing a roughly inverse relationship between  $Z_{TOP}$  and surface  
376 divergence. However, the scale of the changes in  $Z_{TOP}$  are much larger than is typically  
377 observed in subtropical clouds, and changes in  $Z_{TOP}$  appear to correlate better with changes  
378 in cloud cover than with changes in divergence.

379 Turning to the estimate of a boundary layer lapse rate ( $\Gamma_{BL}$ ), we can evaluate the assump-  
380 tion of a constant layer height. As above, the results are highly correlated with variations  
381 in cloud cover, associating decreased boundary layer stability with increases in cloud cover.  
382 This is consistent with the conception of a well-mixed layer for the LC case and a more  
383 decoupled SC boundary layer.

384 The degree of decoupling in each case can be estimated by first calculating the adiabatic  
385 lapse rate ( $\Gamma_{ADB}$ ), which is approximated by assuming 100% cloud cover and using the all-  
386 sky liquid water path to estimate cloud thickness. The overcast assumption results in an  
387 underestimate of cloud thickness and as a result, an overestimate of the boundary layer lapse  
388 rate. Given the cloud thickness and the assumed inversion height, the mean boundary layer  
389 lapse rate is computed by partitioning the layer into cloud (moist adiabat) and sub-cloud  
390 (dry adiabat) layers. Since a well-mixed boundary layer is assumed, the adiabatic lapse rate  
391 will always be greater than the actual lapse rate. The degree of decoupling is thus defined  
392 as the difference between the adiabatic and actual lapse rates ( $\Delta\Gamma = \Gamma_{ADB} - \Gamma_{BL}$ ). Shown  
393 in the bottom plot of Figure 9, the composites of  $\Delta\Gamma$  suggest that the differences in cloud  
394 cover are strongly associated with differences in boundary layer stratification. This implies a  
395 significant difference in the internal dynamics governing the boundary layers of the SC and  
396 LC cases. Interestingly, as with surface divergence, SST advection, and surface fluxes, the  
397 sign of the relationship is reversed in the early part of the trajectory, implying that the LC

398 clouds are initially either more shallow or less coupled than the SC clouds.

399 *e. Lag Correlations and non-linearity in cloud response*

400 The above results suggest an interesting pattern in the time dependence of different  
401 forcings in their association with cloud fraction. Table 1 shows the lagged correlations  
402 between cloud fraction at  $t=0$  and a selection of the variables most strongly associated with  
403 changes in cloud cover. Correlations are computed from samples selected uniformly from  
404 each grid box and each month, using anomalies computed relative to the monthly mean in  
405 each grid box. For each variable, the lag at which a maximum correlation is observed is  
406 highlighted in bold.

407 The correlations provide a convenient means of identifying the lags at which each variable  
408 is most strongly associated with cloud fraction. Note that these lags are not indicative of  
409 a specific moment at which an influence is exerted, but of the time scales over which the  
410 boundary layer responds to each forcing. A pattern is recognizable in several categories of  
411 forcing. LTS and SST are best correlated approximately 36 hours upwind of cloud obser-  
412 vations, consistent with the results of Klein et al. (1995). In contrast, SST advection and  
413 sensible and latent heat fluxes are best correlated at a lag of 6 hours. Specific humidity at  
414 700 hPa has a more varied response, associated with lags ranging from 0 to 12 hours. Finally,  
415 variations in surface divergence are primarily associated with near-instantaneous changes in  
416 cloud properties. Indeed, an interesting outcome of the present study is that subtropical  
417 clouds appear to be subject to large, synoptic-scale variations in subsidence. Overall, these  
418 results suggest a contrast between the thermodynamic and large-scale dynamic influences

419 on cloud fraction, in which the time scales for boundary-layer response to thermodynamic  
420 forcings is long compared to that of dynamic influences.

## 421 **4. Discussion**

422 We begin by summarizing the conditions near the time of observation ( $t \cong -12$  to  $t \cong 12$ ).  
423 By design, the LC cases exhibit significantly greater cloud cover. Accompanying the differ-  
424 ences in cloud cover are a systematic increase in liquid water path and shortwave forcing  
425 relative to the MC and SC cases. Column water vapor (not shown) is also consistently  
426 larger for the LC composite. Combined with cooler SSTs, this suggests that the LC bound-  
427 ary layer is more humid. The cooler SSTs, along with a warmer free troposphere, also result  
428 in a greater stability of the lower atmosphere (LTS) for the LC case.

429 There are two different ways in which this difference in stability can influence cloud  
430 cover. First, given a well-mixed boundary layer, the greater stability will result in a stronger  
431 capping inversion at layer top. This helps to isolate the cloud layer from the warm, dry free  
432 troposphere, and allows the clouds to thicken by decreasing the potential for entrainment  
433 drying. Alternatively, given the same entrainment rate, a warmer free troposphere can result  
434 in increased entrainment drying. However, as shown in Figure 6, the LC case is associated  
435 with a more humid free troposphere. Our calculations indicate that, relative to the SC  
436 case, the excess drying due to the warmer LC free troposphere is more than offset by the  
437 concomitant increase in humidity above the LC boundary layer. As a result, given the same  
438 entrainment rate, the LC case will experience less drying than the SC case. Together with  
439 the implied increase in inversion strength, both influences are consistent with an increase in

440 cloud cover for the LC case relative to the SC case.

441 Surface fluxes also reflect the anticipated differences between dissipating and developing  
442 clouds. The LC composite is associated with stronger cold advection, increased surface wind  
443 speeds, and an increase in surface fluxes. These complement the impacts of LTS and  $q_{700}$  on  
444 entrainment drying by implying a stronger supply of moisture from the surface to the cloud  
445 layer.

446 Finally, we find that large, synoptic-scale changes in divergence are inversely associated  
447 with changes in cloud cover. Specifically, surface divergence and the associated cloud-top  
448 subsidence rate are weaker for the LC case, again promoting either increased growth or a  
449 decreased rate of dilution of the boundary layer. Taken together, the above evidence all  
450 points to a stronger coupling between the surface and cloud layers, and suggests a slower  
451 rate of entrainment drying for the LC clouds. Our estimates of decoupling support this  
452 conclusion, suggesting that the SC boundary layer is significantly more stratified than in the  
453 other two cases.

454 Notably, there are several quantities whose relationship to cloud fraction changes sign  
455 over the course of the trajectory. In particular, surface divergence is weaker for the LC case  
456 at 0 hours but significantly stronger than the other two cases at  $-72$  hours. This reversal is  
457 also seen in the composites of SST advection and surface fluxes, which show weaker surface  
458 exchanges for the LC case at  $t=-72$ . In addition to stronger surface fluxes, the SC boundary  
459 layer is either deeper or more well-mixed at  $t=-72$ . Several authors have noted an association  
460 between increased moisture fluxes and an increased stratification of the cloud and sub-cloud  
461 layers, which can eventually result in decoupling [*e.g.*, Schubert et al. 1979; Bretherton and  
462 Wyant 1997]. Throughout the course of the first 72 hours, the SC composite is consistent

463 with the two-stage model suggested by Wyant et al. (1997). The authors describe a first  
464 stage in which decoupling is driven by increased surface fluxes followed by a second stage in  
465 which continually increasing SSTs contribute to a transition to progressively more vigorous  
466 cumulus convection which increasingly mixes across the inversion, causing the stratocumulus  
467 deck at the boundary layer top to dissipate. This is consistent with the fact that prior to  
468  $t=0$  the SC trajectory experiences SSTs that are substantially greater than those for the LC  
469 composite.

470 The above results can be summarized by proposing the following two scenarios describing  
471 the observed changes in LC and SC clouds. In the case of the SC clouds, advection over a  
472 weaker gradient in SST results in decreased moisture fluxes. Combined with the drier free  
473 troposphere, the boundary layer continues to dry and decouple. For the  $\sim 18$  hours prior  
474 to  $t=0$ , the pronounced increase in divergence produces increased drying and results in a  
475 dissipation of the cloud layer. The LC case, in contrast, is generally more well-mixed. This  
476 implies that the  $\sim 2$  K increase in LTS relative to the SC composite results in a substantially  
477 stronger inversion. The LC clouds also advect over a stronger SST gradient and have stronger  
478 surface winds, prompting greater heat and moisture fluxes from the surface. These are  
479 complemented by an increase in free tropospheric humidity throughout the trajectory, which  
480 acts to moderate the drying due to entrainment as the cloud layer grows. In contrast with  
481 the SC case, the cloud layer remains strongly coupled to the surface throughout the first 72  
482 hours. Finally, a substantial decrease in the divergence rate at  $t=-6$  allows the cloud layer  
483 to thicken as the inversion rises. Both the LC and SC composites return to average values  
484 of cloud cover as the trajectories advect forward into a more cumulus-driven climatology.

## 485 5. Summary and Conclusions

486 We have presented a new method for assessing the Lagrangian impacts of meteorology  
487 on cloud evolution, and applied the analysis to the subtropical cloud regime of the northeast  
488 Atlantic. The method used builds upon the Lagrangian trajectory method introduced by  
489 Mauger and Norris (2007), with the addition of new satellite observations of broadband  
490 fluxes, cloud water, and surface winds. We analyze cloud cover by compositing trajectories  
491 into terciles of low-level cloud fraction, and evaluate the associated changes in meteorological  
492 and cloud properties along trajectories that extend both 72 hours back as well as 72 hours  
493 forward. Atmospheric stability (LTS), surface divergence, free tropospheric humidity ( $q_{700}$ ),  
494 sea surface temperature (SST), and SST advection are all found to contribute strongly to  
495 changes in cloud cover. These quantities serve as proxies for the physical processes that  
496 govern boundary layer evolution.

497 The Lagrangian analysis is also used to identify the time lag at which each of the above  
498 quantities exerts the greatest influence on the evolution of boundary layer clouds. A dis-  
499 tinction is identified between dynamical variables and several thermodynamic conditions,  
500 including LTS, SST, and  $q_{700}$ , which appear to influence cloud properties over longer time  
501 scales. Although many mixed-layer simulations assume steady or slowly-varying divergence,  
502 an important finding of the present work is that large synoptic-scale variations in divergence  
503 are commonplace. These dramatic changes in divergence are found to exert a dominant  
504 influence on cloud properties.

505 By estimating the degree of decoupling, we find evidence that the contrasting evolution  
506 of the large and small cloud cover cases is associated with a notable difference in the stability

507 of the cloud layers. Although our estimate of decoupling is vulnerable to substantial mea-  
508 surement biases, the results are consistent with other factors influencing entrainment drying  
509 and the strength of surface fluxes. Nonetheless, the analysis could be significantly improved  
510 by the inclusion of coincident, independent measurements of boundary layer height. Such  
511 measurements are now possible from the operational Cloud-Aerosol Lidar with Orthogonal  
512 Polarization (CALIOP) cloud height retrieval algorithm. The satellite was not in orbit during  
513 the dates used in the present analysis, but could be used in future analyses.

514 The results presented above reveal the wealth of information that is available in the  
515 Lagrangian analysis developed herein. The present work represents a useful first step in the  
516 Lagrangian characterization of low-level cloud sensitivities. There are many respects in which  
517 the current work can be extended to provide additional information on cloud sensitivities,  
518 such as the inclusion of additional satellite measurements, investigation of other subtropical  
519 regimes, or as in ASTEX (Albrecht et al. 1995), to inform future field campaigns. The  
520 method can also be applied to model output, providing new, focused diagnostic information  
521 on model performance.

522 *Acknowledgments.*

523 This work was supported by an NSF CAREER award, ATM02-38527. The HYSPLIT  
524 model was developed by the National Oceanic and Atmospheric Administrations (NOAA)  
525 Air Resources Laboratory (ARL). MODIS data were obtained from the Level 1 and Atmo-  
526 sphere Archive and Distributions System (LAADS) website, operated by the NASA Goddard  
527 Space Flight Center. CERES data were obtained from the Atmospheric Science Data Center

528 at the NASA Langley Research Center. SSM/I data were obtained from Remote Sensing  
529 Systems, which is sponsored by the NASA Earth Science REASoN DISCOVER Project.  
530 The QuikSCAT Level 2B data were obtained from the Physical Oceanography Distributed  
531 Active Archive Center (PODAAC) at the NASA Jet Propulsion Laboratory, Pasadena, CA.  
532 ECMWF data were obtained from the CISL Data Support Section at the National Center  
533 for Atmospheric Research, Boulder, CO.

## REFERENCES

- 536 Albrecht, B., C. Bretherton, D. Johnson, W. Scubert, and A. Frisch, 1995: The Atlantic  
537 Stratocumulus Transition Experiment: ASTEX. *Bulletin of the American Meteorological*  
538 *Society*, **76 (6)**, 889–904.
- 539 Bretherton, C., E. Klinker, A. Betts, and J. Coakley Jr, 1995: Comparison of Ceilometer,  
540 Satellite, and Synoptic Measurements of Boundary-Layer Cloudiness and the ECMWF  
541 Diagnostic Cloud Parameterization Scheme during ASTEX. *Journal of the Atmospheric*  
542 *Sciences*, **52 (16)**, 2736–2751.
- 543 Bretherton, C. and M. Wyant, 1997: Moisture Transport, Lower-Tropospheric Stability,  
544 and Decoupling of Cloud-Topped Boundary Layers. *Journal of the Atmospheric Sciences*,  
545 **54 (1)**, 148–167.
- 546 Chelton, D. and M. Freilich, 2005: Scatterometer-Based Assessment of 10-m Wind Analyses  
547 from the Operational ECMWF and NCEP Numerical Weather Prediction Models. *Monthly*  
548 *Weather Review*, **133 (2)**, 409–429.
- 549 Garay, M. J., S. P. de Szoeke, and C. M. Moroney, 2008: Comparison of marine stratocumulus  
550 cloud top heights in the southeastern Pacific retrieved from satellites with coincident  
551 ship-based observations. *Journal of Geophysical Research – Atmospheres*, **113**, D18 204,  
552 doi:10.1029/2008JD009 975.

- 553 Harris, J., R. Draxler, and S. Oltmans, 2005: Trajectory model sensitivity to differences in  
554 input data and vertical transport method. *Journal of Geophysical Research - Atmospheres*,  
555 **110**.
- 556 Klein, S., D. Hartmann, and J. Norris, 1995: On the relationships among low-cloud structure,  
557 sea-surface temperature, and atmospheric circulation in the summertime Northeast Pacific.  
558 *Journal of Climate*, **8 (5, Part 1)**, 1140–1155.
- 559 Lewis, G., P. Austin, and M. Szczodrak, 2004: Spatial statistics of marine boundary layer  
560 clouds. *Journal of Geophysical Research - Atmospheres*, **109**.
- 561 Loukachine, K. and N. Loeb, 2003: Application of an Artificial Neural Network Simulation  
562 for Top-of-Atmosphere Radiative Flux Estimation from CERES. *Journal of Atmospheric  
563 and Oceanic Technology*, **20 (12)**, 1749–1757.
- 564 Matheson, M., J. Coakley Jr, and W. Tahnk, 2006: Effects of threshold retrievals on esti-  
565 mates of the aerosol indirect radiative forcing. *Geophysical Research Letters*, **33 (7)**.
- 566 Mauger, G. S., 2008: Synoptic Sensitivities of Subtropical Clouds: Separating Aerosol Effects  
567 from Meteorology. Ph.D. thesis, Scripps Institution of Oceanography – Univ. Calif. San  
568 Diego, <http://repositories.cdlib.org/sio/techreport/83/>.
- 569 Mauger, G. S. and J. R. Norris, 2007: Meteorological bias in satellite esti-  
570 mates of aerosol-cloud relationships. *Geophysical Research Letters*, **34 (16)**, L16 824,  
571 doi:10.1029/2007GL029 952.
- 572 McNoldy, B., P. Ciesielski, W. Schubert, and R. Johnson, 2004: Surface winds, divergence,

573 and vorticity in stratocumulus regions using QuikSCAT and reanalysis winds. *Geophysical*  
574 *Research Letters*, **31**.

575 Milliff, R., J. Morzel, D. Chelton, and M. Freilich, 2004: Wind Stress Curl and Wind  
576 Stress Divergence Biases from Rain Effects on QSCAT Surface Wind Retrievals. *Journal*  
577 *of Atmospheric and Oceanic Technology*, **21 (8)**, 1216–1231.

578 NCAR, 1990: ECMWF TOGA Global Advanced Operational Spectral Analysis, daily 1985-  
579 cont, updated yearly. Published by the CISL Data Support Section at the National Center  
580 for Atmospheric Research, Boulder, CO (ds111.0).

581 Norris, J. and S. Iacobellis, 2005: North Pacific Cloud Feedbacks Inferred from Synoptic-  
582 Scale Dynamic and Thermodynamic Relationships. *Journal of Climate*, **18 (22)**, 4862–  
583 4878.

584 Pincus, R., M. Baker, and C. Bretherton, 1997: What Controls Stratocumulus Radiative  
585 Properties? Lagrangian Observations of Cloud Evolution. *Journal of the Atmospheric*  
586 *Sciences*, **54 (17)**, 2215–2236.

587 Platnick, S., M. King, S. Ackerman, W. Menzel, B. Baum, J. Riedi, and R. Frey, 2003:  
588 The MODIS cloud products: Algorithms and examples from Terra. *IEEE Transactions*  
589 *on Geoscience and Remote Sensing*, **41 (2)**, 459–473, doi:{10.1109/TGRS.2002.808301}.

590 Rozendaal, M. and W. Rossow, 2003: Characterizing Some of the Influences of the General  
591 Circulation on Subtropical Marine Boundary Layer Clouds. *Journal of the Atmospheric*  
592 *Sciences*, **60 (5)**, 711–728.

593 Schubert, W., J. Wakefield, E. Steiner, and S. Cox, 1979: Marine Stratocumulus Convection.  
594 Part I: Governing Equations and Horizontally Homogeneous Solutions. *Journal of the*  
595 *Atmospheric Sciences*, **36 (7)**, 1286–1307.

596 Stevens, B., A. Beljaars, S. Bordoni, C. Holloway, M. Koehler, S. Krueger, V. Savic-Jovicic,  
597 and Y. Zhang, 2007: On the structure of the lower troposphere in the summertime stra-  
598 tocumulus regime of the northeast Pacific. *Monthly Weather Review*, **135 (3)**, 985–1005,  
599 doi:{10.1175/MWR3427.1}.

600 Stohl, A., M. Hittenberger, and G. Wotawa, 1998: Validation of the lagrangian particle  
601 dispersion model FLEXPART against large-scale tracer experiment data. *Atmospheric*  
602 *Environment*, **32 (24)**, 4245–4264.

603 Stohl, A. and P. Seibert, 1998: Accuracy of trajectories as determined from the conser-  
604 vation of meteorological tracers. *Quarterly Journal of the Royal Meteorological Society*,  
605 **124 (549)**, 1465–1484.

606 Wentz, F., 1997: A well-calibrated ocean algorithm for SSM/I. *Journal of Geophysical Re-*  
607 *search - Atmospheres*, **102 (C4)**, 8703–8718.

608 Wielicki, B. and L. Parker, 1992: On the determination of cloud cover from satellite sen-  
609 sors: the effect of sensor spatial resolution. *Journal of Geophysical Research, Atmospheres*,  
610 **97 (12)**, 12 799–12 823.

611 Wyant, M., C. Bretherton, H. Rand, and D. Stevens, 1997: Numerical Simulations and  
612 a Conceptual Model of the Stratocumulus to Trade Cumulus Transition. *Journal of the*  
613 *Atmospheric Sciences*, **54 (1)**, 168–192.

TABLE 1. Lagged correlations between low-level cloud fraction ( $CF_{L/Q}$ ) at the time of observation (0 hours) for the variables and time lags listed below. Blank cells indicate that retrievals are not available at the given lag.

Variable	t = 0 hours	t = 6 hours	t = 24 hours	t = 36 hours	t = 48 hours
LWP <sub>f15</sub> *	<b>0.539 (0.511, 0.567)</b>	—	0.162 (0.124, 0.199)	0.084 (0.047, 0.122)	0.054 (0.017, 0.091)
LTS	0.122 (0.094, 0.150)	0.187 (0.159, 0.214)	0.295 (0.269, 0.321)	<b>0.326 (0.300, 0.351)</b>	0.279 (0.253, 0.305)
SST	-0.114 (-0.142, -0.086)	-0.155 (-0.183, -0.127)	<b>-0.189 (-0.217, -0.162)</b>	-0.184 (-0.211, -0.156)	-0.151 (-0.179, -0.123)
F <sub>SH</sub>	<b>-0.086 (-0.114, -0.058)</b>	-0.073 (-0.147, 0.002)	0.015 (-0.014, 0.043)	0.035 (0.006, 0.063)	0.018 (-0.010, 0.046)
F <sub>LH</sub>	-0.027 (-0.055, 0.001)	<b>-0.073 (-0.148, 0.002)</b>	-0.001 (-0.030, 0.027)	0.050 (0.022, 0.078)	<b>0.090 (0.062, 0.118)</b>
$\Delta$ SST	-0.078 (-0.106, -0.050)	<b>-0.128 (-0.156, -0.100)</b>	-0.086 (-0.115, -0.058)	-0.026 (-0.054, 0.003)	0.010 (-0.019, 0.039)
q <sub>700</sub>	<b>0.123 (0.095, 0.151)</b>	0.124 (0.096, 0.152)	0.090 (0.062, 0.118)	0.068 (0.040, 0.097)	0.063 (0.034, 0.091)
WVP <sub>f15</sub>	<b>0.109 (0.069, 0.148)</b>	—	0.044 (0.006, 0.082)	0.042 (0.004, 0.079)	0.053 (0.015, 0.090)
DIV <sub>Q</sub> <sup>†</sup>	<b>-0.108 (-0.156, -0.060)</b>	—	0.031 (-0.018, 0.079)	—	0.063 (0.016, 0.110)
DIV <sub>E</sub>	<b>-0.162 (-0.189, -0.134)</b>	-0.138 (-0.165, -0.110)	0.011 (-0.018, 0.039)	0.043 (0.015, 0.071)	0.077 (0.049, 0.105)
$\omega_{700}$	<b>-0.117 (-0.144, -0.089)</b>	-0.096 (-0.124, -0.068)	-0.027 (-0.056, 0.001)	-0.009 (-0.037, 0.019)	0.004 (-0.025, 0.032)

\*Overpass times for the DMSP f15 satellite do not match Terra overpass times exactly, so that the LWP<sub>f15</sub> correlations are effectively lagged by an additional 1-2 hours.

<sup>†</sup>Overpass times for the QuikScat satellite do not match Terra overpass times, so the DIV<sub>Q</sub> correlations are lagged by approximately 6 additional hours relative to the lag denoted in each column.

## 614 List of Figures

- 615 1 The study region used in the present work, outlined in thick black lines (24-  
616 40N, 35-10W). The thin black lines denote the grid boxes used to ensure even  
617 sampling throughout the domain. Climatologies of MODIS low-level cloud  
618 cover ( $CF_{LIQ}$ ) and ECMWF 10m wind speed are shown for the dates used in  
619 this study (JJA 2000-2006). 33
- 620 2 Histogram of MODIS low-level cloud fraction. The y-axis denotes the fraction  
621 of all points that fall into each bin, and the dashed lines delineate terciles (SC,  
622 MC, and LC) in cloud fraction. 34
- 623 3 Composite trajectories for the large (LC, thin black lines), middle (MC,  
624 medium-width dark gray lines), and small (SC, thick light gray lines) terciles  
625 of MODIS low-level cloud fraction. Error bars denote the 95% confidence  
626 limits obtained using the bootstrap method described in the text. Land areas  
627 are shaded in gray. 35
- 628 4 Composites trajectories for overlap-corrected MODIS low-level cloud fraction  
629 ( $CF_{LIQ}$ ) and CERES all-sky top-of-atmosphere net shortwave flux ( $F_{SW}$ ,  $W$   
630  $m^{-2}$ ). 36
- 631 5 As in Figure 4 except showing different measures of cloud water path. All  
632 variables are displayed in units of  $g m^{-2}$ . Displayed from top to bottom are:  
633 MODIS in-cloud LWP, MODIS all-sky LWP, and SSM/I all-sky LWP from  
634 the f15 satellite. 37

- 635 6 As in Figure 4 except showing lower tropospheric stability (LTS, defined as  
636  $\theta_{700} - \theta_{SFC}$ , K), sea surface temperature (K), and 700 hPa temperature ( $T_{700}$ ,  
637 K) and moisture ( $q_{700}$ ,  $\text{g kg}^{-1}$ ), all obtained from ECMWF analyses. 38
- 638 7 As in Figure 4 except showing the rate of SST change ( $\Delta\text{SST} \times 10^{-5} \text{ K s}^{-1}$ ),  
639 10m wind speed ( $\text{m s}^{-1}$ ), surface sensible heat flux ( $F_{SH} \text{ W m}^{-2}$ ) and surface  
640 latent heat flux ( $F_{LH} \text{ W m}^{-2}$ ), all obtained from ECMWF analyses. 39
- 641 8 Composite trajectories showing QuikScat and ECMWF surface divergence  
642 ( $\text{DIV}_{QSCAT}$ ,  $\text{DIV}_{ECMWF}$ ,  $\times 10^{-6} \text{ s}^{-1}$ ), and ECMWF 700 hPa pressure vertical  
643 velocity ( $\omega_{700}$ ,  $\text{Pa s}^{-1}$ ) 40
- 644 9 As in Figure 4 except showing MODIS retrievals of cloud top temperature  
645 ( $T_{TOP}$ , K) and derived cloud top height ( $Z_{TOP}$ , defined as  $(SST - T_{TOP})/6.5$ ,  
646 km), boundary-layer lapse rate ( $\Gamma_{BL} = \Gamma_{ADB} - \Gamma_{BL}$ ,  $\text{K km}^{-1}$ ), and deviation  
647 of the lapse rate from adiabatic ( $\Delta\Gamma$ ,  $\text{K km}^{-1}$ ). 41

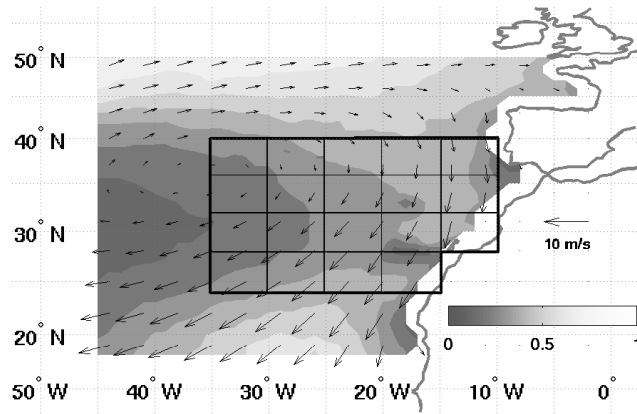


FIG. 1. The study region used in the present work, outlined in thick black lines (24-40N, 35-10W). The thin black lines denote the grid boxes used to ensure even sampling throughout the domain. Climatologies of MODIS low-level cloud cover ( $CF_{LIQ}$ ) and ECMWF 10m wind speed are shown for the dates used in this study (JJA 2000-2006).

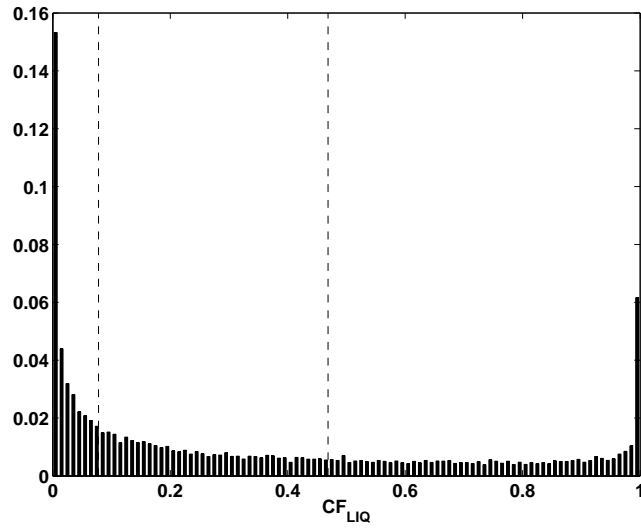


FIG. 2. Histogram of MODIS low-level cloud fraction. The y-axis denotes the fraction of all points that fall into each bin, and the dashed lines delineate terciles (SC, MC, and LC) in cloud fraction.

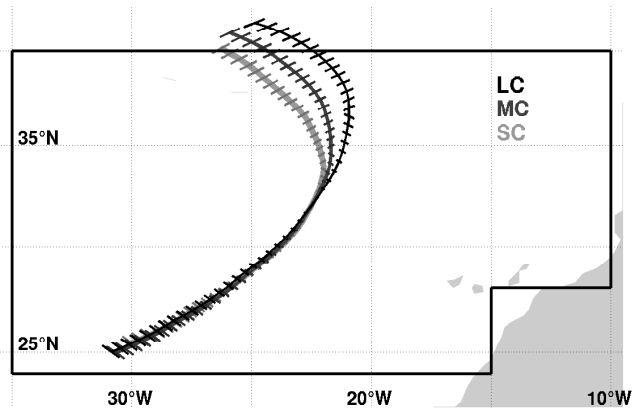


FIG. 3. Composite trajectories for the large (LC, thin black lines), middle (MC, medium-width dark gray lines), and small (SC, thick light gray lines) terciles of MODIS low-level cloud fraction. Error bars denote the 95% confidence limits obtained using the bootstrap method described in the text. Land areas are shaded in gray.

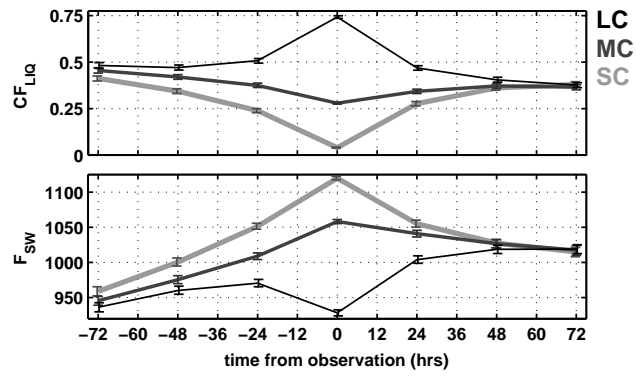


FIG. 4. Composites trajectories for overlap-corrected MODIS low-level cloud fraction ( $CF_{LIQ}$ ) and CERES all-sky top-of-atmosphere net shortwave flux ( $F_{SW}$ ,  $W m^{-2}$ ).

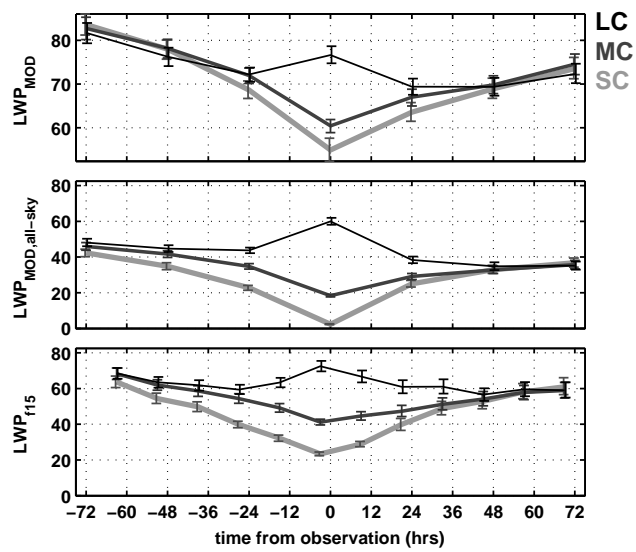


FIG. 5. As in Figure 4 except showing different measures of cloud water path. All variables are displayed in units of  $\text{g m}^{-2}$ . Displayed from top to bottom are: MODIS in-cloud LWP, MODIS all-sky LWP, and SSM/I all-sky LWP from the f15 satellite.

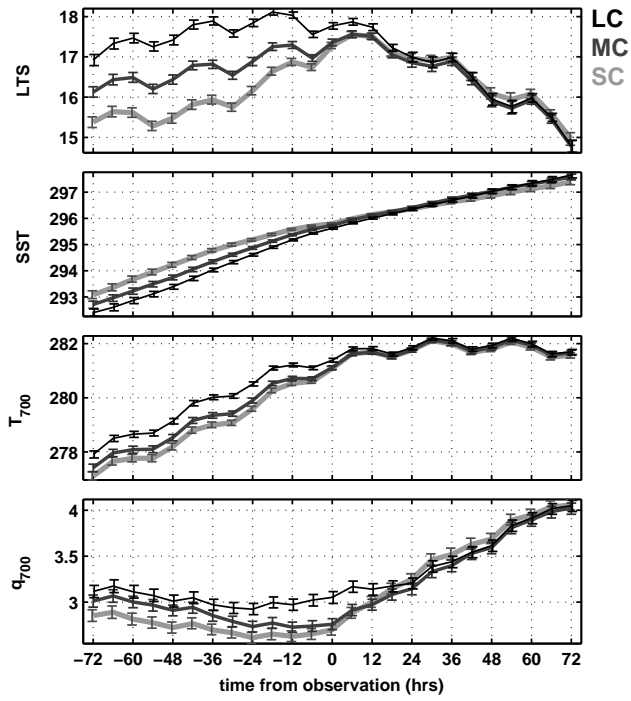


FIG. 6. As in Figure 4 except showing lower tropospheric stability (LTS, defined as  $\theta_{700} - \theta_{SFC}$ , K), sea surface temperature (K), and 700 hPa temperature ( $T_{700}$ , K) and moisture ( $q_{700}$ ,  $\text{g kg}^{-1}$ ), all obtained from ECMWF analyses.

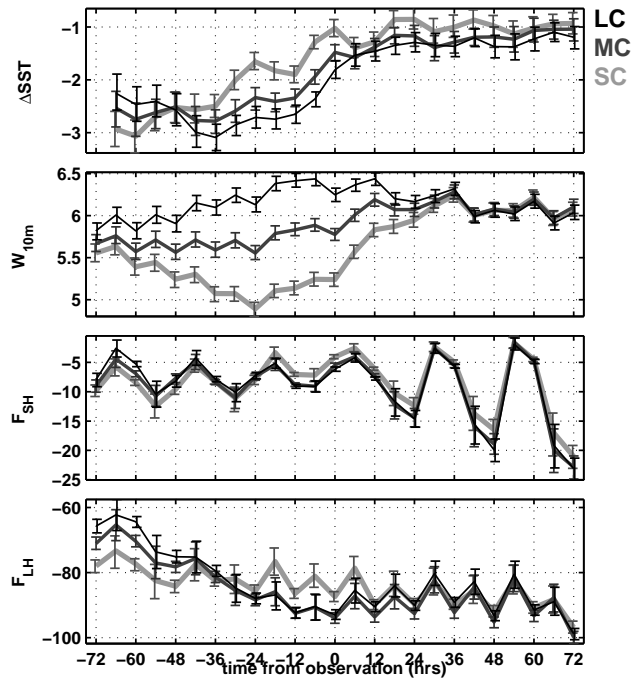


FIG. 7. As in Figure 4 except showing the rate of SST change ( $\Delta\text{SST} \times 10^{-5} \text{ K s}^{-1}$ ), 10m wind speed ( $\text{m s}^{-1}$ ), surface sensible heat flux ( $F_{SH} \text{ W m}^{-2}$ ) and surface latent heat flux ( $F_{LH} \text{ W m}^{-2}$ ), all obtained from ECMWF analyses.

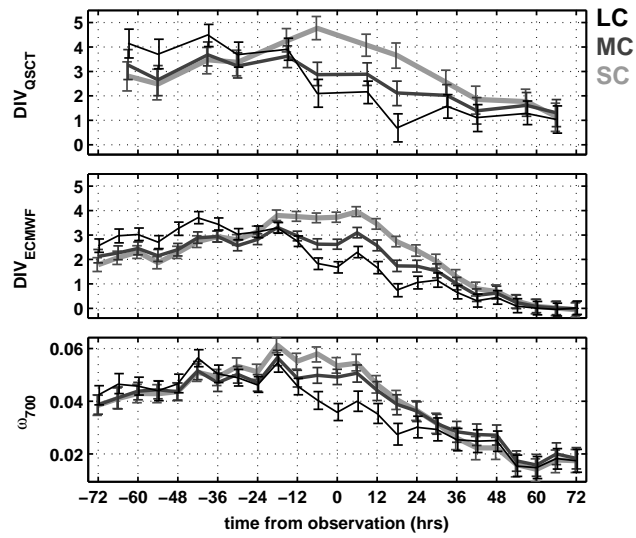


FIG. 8. Composite trajectories showing QuikScat and ECMWF surface divergence ( $DIV_{QSCT}$ ,  $DIV_{ECMWF}$ ,  $\times 10^{-6} \text{ s}^{-1}$ ), and ECMWF 700 hPa pressure vertical velocity ( $\omega_{700}$ ,  $\text{Pa s}^{-1}$ )

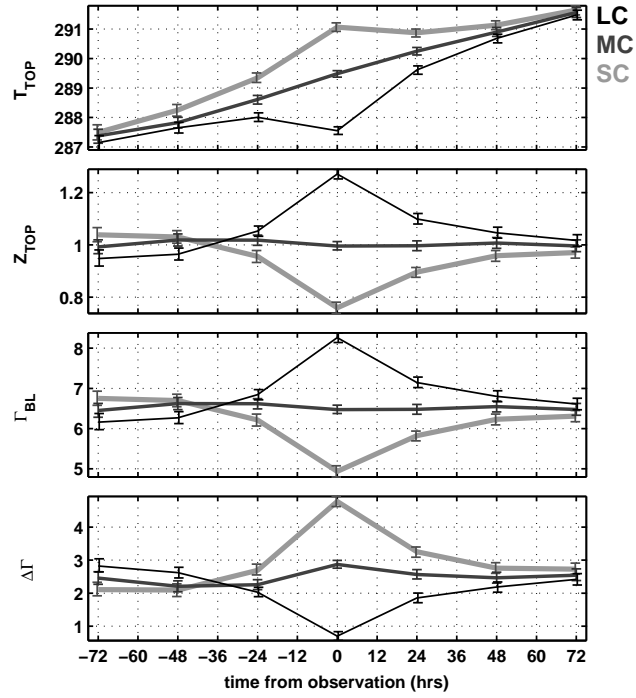


FIG. 9. As in Figure 4 except showing MODIS retrievals of cloud top temperature ( $T_{TOP}$ , K) and derived cloud top height ( $Z_{TOP}$ , defined as  $(SST - T_{TOP})/6.5$ , km), boundary-layer lapse rate ( $\Gamma_{BL} = \Gamma_{ADB} - \Gamma_{BL}$ ,  $K km^{-1}$ ), and deviation of the lapse rate from adiabatic ( $\Delta\Gamma$ ,  $K km^{-1}$ ).